

pubs.acs.org/JPCC Article

Phase-Controlled Deposition of Ru on Pd Nanocrystal Templates: Effects of Particle Shape and Size

Annemieke Janssen, Quynh N. Nguyen, Zhiheng Lyu, Veronica Pawlik, Chenxiao Wang, and Younan Xia*



Cite This: J. Phys. Chem. C 2023, 127, 1280-1291



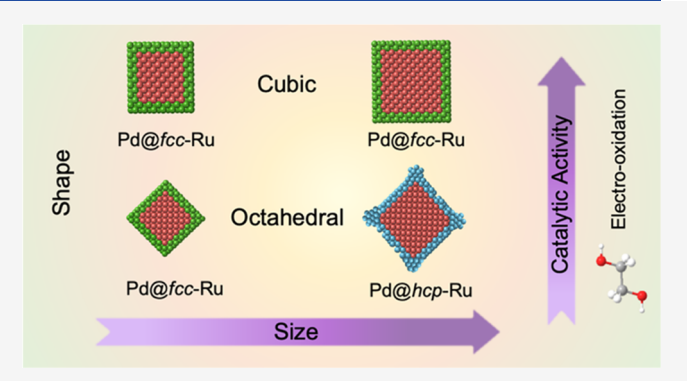
ACCESS I

III Metrics & More

Article Recommendations

sı Supporting Information

ABSTRACT: Template-directed growth has been widely used for the phase-controlled synthesis of metal nanocrystals, but much remains to be discovered about the mechanistic details. In this work, we systematically investigate the roles played by the shape and size of Pd nanocrystal templates in controlling the crystal phase taken by the deposited Ru overlayers. For Pd cubic nanocrystals, a face-centered cubic (fcc) Ru shell is always favored when the particle size is varied in the range of 6–25 nm. In the case of Pd octahedral nanocrystals, we observe a size dependence, with 14-nm octahedra giving fcc-Ru but 20- and 26-nm octahedra resulting in hexagonal close-packed (hcp) Ru. This trend can be attributed to their difference in surface atomic arrangement, as the {100} facets on a cubic template cannot be matched by any facet of hcp-Ru,



forcing the deposited Ru to take the fcc phase. In contrast, the {111} facets on an octahedral template can be matched by the {0001} facets of hcp-Ru, allowing the deposited Ru to take either an hcp or fcc phase. The crystal phase taken by the Ru shell is determined by the relative contributions from the surface and bulk energies of the deposited fcc- and hcp-Ru phases. Additionally, the water content in the reaction mixture also plays an important role in affecting the crystal phase taken by the Ru shell by altering the reduction kinetics. When tested as catalysts toward ethylene glycol oxidation, the fcc-Ru outperforms hcp-Ru, while the cubic shape is advantageous over the octahedral counterpart.

■ INTRODUCTION

Compared with other parameters such as size, shape, and internal structure, 1-9 controlling the crystal structure or phase taken by noble-metal nanocrystals, a feature known as polymorphism, is a relatively recent endeavor. 10,11 Since all research on the phase-controlled synthesis of noble-metal nanocrystals was reported within the past decade, 12-15 there is still a lot to be learned about the mechanistic details responsible for phase engineering, similar to the situation in the early days of shape control. Currently, one of the most commonly used methods for phase control is template-directed (or seed-mediated) growth, in which a nanocrystal in a specific crystal structure serves as a template to govern the heterogeneous nucleation and deposition of a different metal with a distinct native crystal phase to impose its crystal structure on the deposited overlayers. 11,16 As a major hallmark of template-directed growth, one can systematically evaluate all parameters that affect phase evolution for the achievement of rational synthesis of metal nanocrystals with desired crystal structures. To this end, a number of studies have begun to explore the effects of reduction kinetics, overlayer thickness, and particle size on phase evolution during a template-directed synthesis. 15,17-20 However, the influence of the template's shape on the crystal phase of the deposited overlayers remains elusive.

Ruthenium (Ru) is among the most extensively investigated metals for phase control by template-directed growth. ^{17,21–25} This metal is naturally found in the hexagonally close-packed (hcp) phase, although face-centered cubic (fcc)-Ru has been obtained through a careful control of its deposition on Pd nanocrystal templates. Specifically, fcc-Ru can be deposited as conformal shells on a variety of Pd nanocrystal templates, including those with cubic, octahedral, and icosahedral shapes. ^{17,21–24} Despite the successful syntheses, the mechanism behind phase control, such as the role played by the shape, and thus faceting, or the interplay between size and shape of the template, has mostly been overlooked. Since the faceting of a nanocrystal corresponds to a specific arrangement of atoms on the surface, this parameter could have a major

Received: December 16, 2022 Revised: December 23, 2022 Published: January 6, 2023





impact on the outcome of a template-directed synthesis.²⁶ In a recent study involving Pd nanoplates, it was also found that the crystal phase taken by the deposited Ru overlayers depended on the lateral size of the template, with 12-nm plates giving fcc-Ru while 18-, 22-, and 26-nm plates resulted in hcp-Ru.²⁷ In this case, although Ru can be epitaxially deposited on the basal planes of a Pd nanoplate to take either a stable hcp phase (low in bulk energy) or metastable fcc phase (high in bulk energy), the difference in stacking order will lead to jagged hcp facets (high in surface energy) or smooth fcc facets (low in surface energy) on the side faces, respectively. As the lateral size of the nanoplate is varied, the proportions of basal and side faces will change, and so will the crystal phase, depending on the relative contributions from the surface and bulk energies. Such a dependence on the faceting (related to surface structure) or size is expected to occur in templates of other shapes, especially those primarily enclosed by a single type of facet, which may serve as a simpler model system to investigate this concept. For example, the deposition of Ru on Pd cubic and octahedral nanocrystals, which are largely covered by {100} and {111} facets to give distinct surface atomic arrangements, may lead to different crystal phases for the deposited Ru due to the symmetry mismatch between the facets of fcc and hcp structures. In comparison, templates enclosed by mixed facets, such as cuboctahedral or plate-like nanocrystals, would make it challenging to elucidate the effect of surface atomic arrangement on phase control while having it discerned from the impact of particle size.

This work aims to investigate the effects of particle shape and size by conformally depositing Ru on Pd cubic and octahedral nanocrystals with different edge lengths, and then analyzing the phases taken by the Ru overlayers. We synthesized and characterized Pd@Ru cubic nanocrystals and Pd@Ru octahedral nanocrystals of 6-25 and 14-26 nm, respectively, in edge length. For the Ru deposited on the Pd cubic nanocrystals, the shell took an fcc phase regardless of the particle size. In contrast, for the Pd octahedral nanocrystals, the Ru overlayers only inherit an fcc phase on the 14-nm Pd template while both 20- and 26-nm templates gave an hcp phase, displaying a clear dependence on particle size. In both the cubic and octahedral systems, the crystal phase of Ru shell was also affected by the presence of water in the reaction mixture due to the associated acceleration of reduction kinetics. When the Pd@Ru nanocrystals were tested as catalysts toward the ethylene glycol oxidation reaction (EGOR), the samples with an fcc shell were found to outperform the hcp counterparts, with the activity showing dependences on particle size and shape as well. Overall, by elucidating the roles played by the shape and size of nanocrystal templates in a phase-controlled synthesis, we gained a better understanding of the mechanisms underlying polymorphism.

■ EXPERIMENTAL SECTION

Chemicals and Materials. Poly(vinyl pyrrolidone) (PVP, with an average molecular weight of 55,000), ascorbic acid (AA, 99%), sodium tetrachloropalladate (Na₂PdCl₄, 98%), potassium bromide (KBr, 99%), potassium chloride (KCl, 99%), ruthenium(III) chloride (RuCl₃, 99.9%), potassium hydroxide (KOH, 85%), hydrochloric acid (HCl, 37%), palladium chloride (PdCl₂, 60% metal basis), potassium iodide (KI, 99%), hexadecyltrimethylammonium bromide (CTAB, 98%), formaldehyde (HCHO, 37%), copper sulfate (CuSO₄,

99%), sulfuric acid (H_2SO_4 , 99%), ferric chloride (FeCl₃, 97%), and Nafion (5 wt %) were all obtained from Sigma-Aldrich. Ethanol (99.5%) was obtained from VWR. Ethylene glycol (EG, 99%) was ordered from J. T. Baker. Carbon black was purchased from Cabot (Vulcan XC72). All aqueous solutions were prepared using deionized water with a resistivity of 18.2 $M\Omega$ ·cm at room temperature.

Characterizations. All transmission electron microscopy (TEM) images were captured with a Hitachi HT7700 microscope. The sample was prepared by adding a drop of colloidal suspension onto a carbon-coated Cu grid, followed by drying at ambient temperature. X-ray diffraction (XRD) patterns were recorded on a Panalytical XPert PRO Alpha-1 diffractometer. High-angle annular dark-field scanning transmission electron microscopy (HAADF-STEM) images were taken on a Hitachi HD2700 microscope. Inductively coupled plasma mass spectroscopy (ICP-MS) analysis was conducted using a PerkinElmer instrument (NexION 300Q).

Synthesis of 6-, 10-, and 18-nm Pd Cubic Nanocrystals. The cubic nanocrystals with edge lengths of *ca.* 18 nm were synthesized using a previously reported protocol. ²⁸ In a typical synthesis, 8 mL of an aqueous solution containing 105 mg of PVP, 60 mg of AA, and 600 mg of KBr was heated in an oil bath held at 80 °C for 10 min. Next, 3 mL of aqueous Na₂PdCl₄ (19 mg/mL) was injected in one shot. The reaction was allowed to proceed for 3 h. The particles were collected through centrifugation at 12,000 rcf and washed three times with water prior to redispersion in water or EG for further use. To synthesize 6- and 10-nm cubic nanocrystals, the same protocol was used, except that the 600 mg of KBr was replaced by 185 mg of KCl plus 5 mg of KBr and 300 mg of KBr, respectively.

Synthesis of 25-nm Pd Cubic Nanocrystals. The synthesis was slightly modified from a published protocol. First, an aqueous H_2PdCl_4 solution was prepared by mixing 0.0177 g of $PdCl_2$ with 10 mL of 0.2 M HCl. Next, 50 mg of CTAB was mixed with 9.3 mL of water under sonication, followed by the introduction of 500 μ L of the H_2PdCl_4 solution. Under stirring, 0.2 mL of aqueous NaI (15 mg/mL) was added. The reaction mixture was heated for 5 min in an oil bath held at 100 °C, followed by the introduction of 200 μ L of aqueous AA (7 mg/mL). The reaction was allowed to proceed for 30 min. The particles were collected by centrifugation at 12,000 rcf and washed with water three times prior to redispersion in water or EG for further use.

Synthesis of 14-, 20-, and 26-nm Pd Octahedral Nanocrystals. The octahedral nanocrystals were synthesized according to a published protocol.30 To generate 14-nm octahedral nanocrystals, 8 mL of an aqueous solution containing 105 mg of PVP, 100 μ L of formaldehyde, and 0.3 mL of an aqueous suspension of the 6-nm Pd cubic nanocrystals (ca. 2.5 mg/mL) were heated while stirring in an oil bath held at 60 °C. Next, 2 mL of aqueous Na₂PdCl₄ (9.33 mg/mL) was injected in one shot, and the reaction was allowed to proceed for 3 h. The particles were collected by centrifugation at 12,000 rcf and washed three times with water before they were dispersed in water or EG for further use. To synthesize 20- or 26-nm Pd octahedral nanocrystals, the same protocol was used except for the replacement of the seeds by the 10- or 18-nm Pd cubic nanocrystals (ca. 2.5 mg/mL) and the use of 3 mL of aqueous Na₂PdCl₄.

Synthesis of Pd@Ru Core—Shell Nanocrystals. In a typical synthesis, 1 mL of the as-obtained Pd nanocrystal seed

(dispersed in water at *ca.* 2.5 mg/mL for the 6-, 10-, and 18-nm cubic samples, *ca.* 0.75 mg/mL for the 25-nm cubic sample, *ca.* 7.5 mg/mL for the 14-nm octahedral sample, and *ca.* 10 mg/mL for the 20- and 26-nm octahedral samples) were collected by centrifugation and then mixed with 1 mL EG under sonication to obtain the seed suspension in EG. Next, 12.5 mg of AA, 10 mg of KBr, 100 mg of PVP, and 1 mL of the seed in EG were mixed with 2.25 mL of EG and heated in an oil bath held at 180 °C for 30 min. Meanwhile, Ru(III) precursor solutions were prepared for the different types of seeds by dissolving a specific amount of RuCl₃ in EG to tune the ratio of metal precursor to seed according to Table 1.

Table 1. Summary of the Precursor Solutions Involved in the Synthesis of Pd@Ru Core—Shell Nanocrystals Featuring Different Shapes and Sizes^a

seed	RuCl ₃ (mg)	EG (mL)	$\begin{array}{c} RuCl_3 \\ (mg/mL) \end{array}$	Ru precursor/seed ratio (mg/mg)
6-nm cubic nanocrystals	0.075	3	0.025	0.06
10-nm cubic nanocrystals	0.80	15	0.05	0.32
18-nm cubic nanocrystals	1.00	20	0.05	0.4
25-nm cubic nanocrystals	0.05	2	0.025	0.06
14-nm octahedral nanocrystals	0.05	2	0.025	0.006
20-nm octahedral nanocrystals	0.10	5	0.02	0.07
26-nm octahedral nanocrystals	0.15	7.5	0.02	0.015

^aNote that the temperature $(180 \, ^{\circ}\text{C})$ and volume $(1 \, \text{mL})$ of the seed suspension (in EG) were kept the same.

The precursor solution was injected at 0.5 mL/h, and the reaction was allowed to proceed for 2 h after all of the precursor had been added. The resulting nanocrystals were washed with acetone (acetone/EG = 3:1, v/v), collected by centrifugation at 10,000 rcf, and washed three additional times with ethanol before being redispersed in ethanol for further use. To vary the injection rate, the precursor was added in one shot or at other rates from 0.5 to 4 mL/h using a syringe pump. To study the effects of water, 1 mL of water was added into the reaction container, or the precursor was dissolved in the water/EG mixture ($1:1 \ v/v$), or by dispersing the seed in water. To determine the effects of reaction temperature, the oil bath was also set to 150, 165, and 195 °C, respectively.

Etching of the Pd@Ru Core—Shell Nanocrystals. To etch the Pd core, the Pd@Ru nanocrystals were mixed with 5 mL of an aqueous solution containing 30 mg of FeCl₃, 50 mg of PVP, and 300 mg of KBr, and heated at 100 °C for 1 h. The resulting solid products were collected by centrifugation and washed once with ethanol and twice with water before redispersion in water for further use.

Catalytic Measurements. The catalyst ink was prepared by sonicating carbon black in ethanol at 1 mg/mL for 1 h. The ethanol suspension of Pd@Ru cubic or octahedral nanocrystals was added under sonication at approximately 20% total loading by weight. After 1 h of sonication, the solid was collected through centrifugation at 6000 rcf for 10 min and washed three times with ethanol. Finally, the solid was redispersed in a mixture of 990 μ L of ethanol and 10 μ L of Nafion.

Electrochemical measurements were conducted on a CHI 600E potentiostat electrochemical workstation using a three-electrode cell at room temperature. The working electrode was a glassy carbon electrode (GC, 5 mm in diameter), the counter electrode was a Pt wire, and the reference electrode was a silver/silver chloride (Ag/AgCl) or saturated calomel (SCE) electrode. To prepare the GC electrode, it was polished with 0.3- μ m and then 0.05- μ m Al₂O₃ powders, followed by washing with water and ethanol. Finally, 10 μ L of the catalyst ink was dropped on the GC electrode and allowed to dry at ambient temperature.

To prepare for EGOR, all solutions were purged with Ar. The catalyst surface was cleaned by cycling the potential 40–60 times between -0.8 and 0.4 V (vs Ag/AgCl) at 0.5 mV/s in 0.1 M aqueous KOH. To test the activity, the potential was cycled 20 times between -0.8 and 0.4 V at 50 mV/s in an aqueous electrolyte containing 1 M KOH and 1 M EG.

We used Cu underpotential deposition (UPD) to measure the electrochemical surface area (ECSA). The catalyst surface was cleaned by cycling 20 times between -0.24 and 0.48 V (vs SCE) in 0.5 M aqueous $\rm H_2SO_4$. For Cu UPD, the potential was held at 0.156 V for 100 s, followed by sweeping the potential from 0.156 to 0.4 V in an aqueous electrolyte containing 0.05 M $\rm H_2SO_4$ and 0.002 M $\rm CuSO_4$. An assumed value of 420 $\mu\rm C/cm$ for a full Cu monolayer coverage on Ru surfaces was used to calculate the ECSA through integration of the Cu UPD stripping charges.

■ RESULTS AND DISCUSSION

This study focuses on the effects of particle shape and size on the packing of atoms deposited during the template-directed growth. We chose to investigate the deposition of Ru on fcc-Pd cubic and octahedral nanocrystals of various sizes, as the surfaces of these templates are predominantly covered by {100} and {111} facets, respectively. These different types of facets on the fcc-Pd templates correspond to unique atomic arrangements on their surfaces. Specifically, the {100} facets correspond to a square arrangement of atoms with C4 symmetry, while the {111} facets relate to a triangular arrangement with C₃ symmetry. The C₄ symmetry of the $\{100\}$ facets cannot be matched by any facet of the intrinsically stable hcp phase of Ru. ²⁶ Thus, the deposited Ru overlayers on a cubic template must take an fcc phase to ensure alignment between the lattices of the core and the shell. In other words, layer-by-layer deposition of hcp-Ru on an fcc-Pd cubic template is prohibited by the mismatch in atomic arrangement. Consequently, the Ru overlayers only take an fcc phase when epitaxially deposited on a cubic template, regardless of particle

For the deposition involving the $\{111\}$ facets on an octahedral template, the situation is more complicated. The C_3 symmetry of the $\{111\}$ facets on an fcc template is well matched by the C_3 symmetry of the $\{0001\}$ facets of an hcp lattice. Consequently, it is possible to deposit either fcc- or hcp-Ru overlayers on fcc- $\{111\}$ facets. The preference for either crystal phase is likely dependent on the template's size and thus proportions of edges and side faces. When an fcc-Ru shell is deposited on an fcc-Pd octahedral template, the matching in crystal structure between the core and the shell can give rise to smooth overlayers on both side faces and edges (Figure S1A). Thus, the resulting particle should have a low surface energy (due to smooth edges), but a high bulk energy (due to the formation of metastable fcc-Ru). 16,27,31

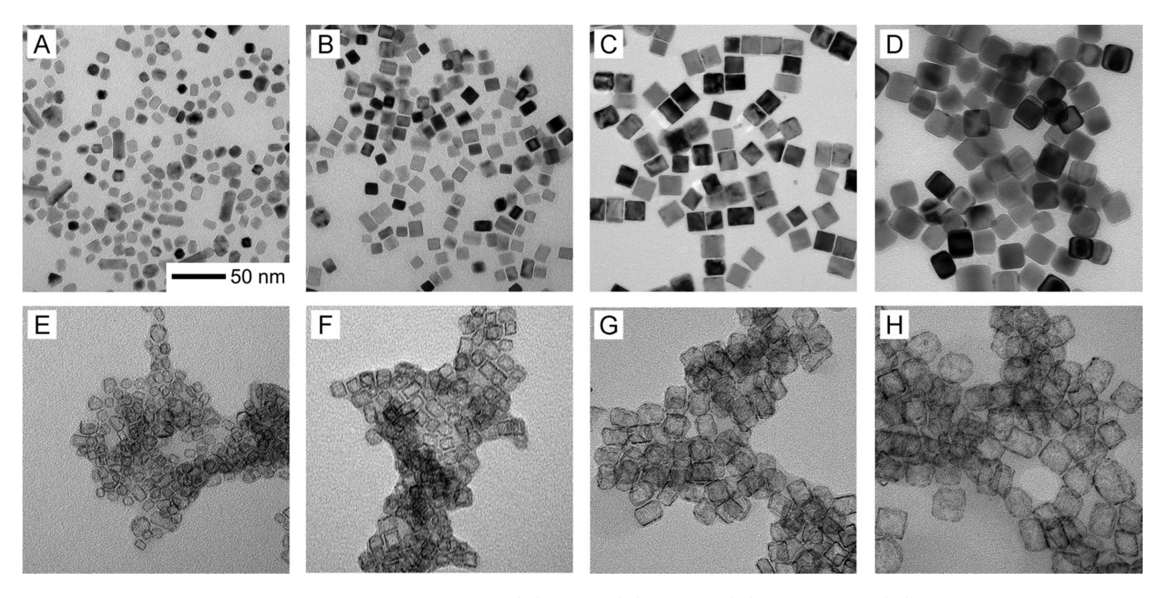


Figure 1. TEM images of the Pd@Ru nanocrystals derived from (A) 6-nm, (B) 10-nm, (C) 18-nm, and (D) 25-nm Pd cubic templates, and (E—H) the corresponding Ru nanocages after selective removal of Pd from the core by wet etching. The scale bar in (A) applies to all panels.

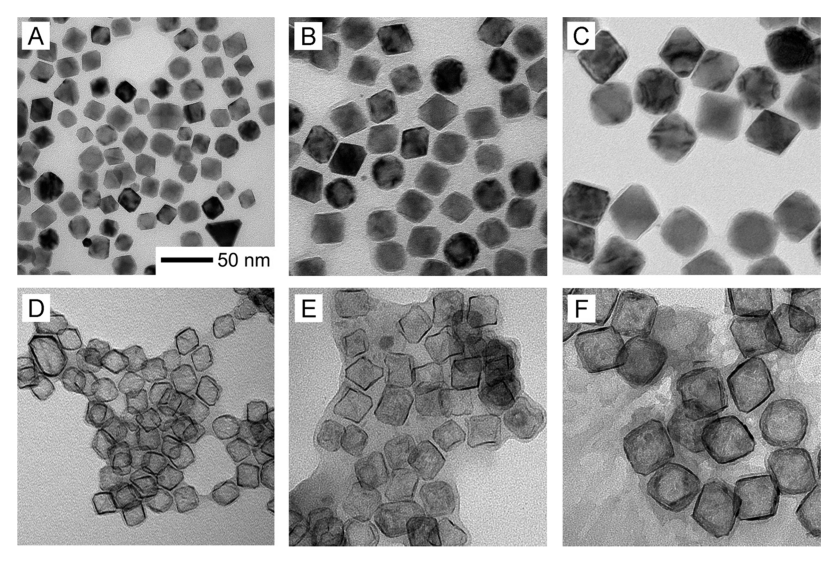


Figure 2. TEM images of the Pd@Ru nanocrystals derived from (A) 14-nm, (B) 20-nm, and (C) 26-nm Pd octahedral templates, and (D-F) the corresponding Ru nanocages after selective removal of Pd from the core by wet etching. The scale bar in (A) applies to all panels.

This crystal phase is favorable when a high percentage of the total surface is contributed by edges, such as in the case of templates with smaller sizes. In contrast, when an hcp-Ru shell is deposited on an fcc-Pd octahedral template, the surface energy of the edges will be increased. This high surface energy can be ascribed to the inherent misalignment between the ABAB stacking sequence characteristic of hcp packing and the ABCABC stacking of the fcc lattice, causing the edges to be jagged and full of undercoordinated atoms, although hcp-Ru can smoothly cover the fcc-{111} side faces (Figure S1B). Consequently, the high surface energy (due to jagged edges) and low bulk energy (due to the formation of thermodynamically stable hcp-Ru) would make the deposition of an hcp-Ru shell more favorable on larger templates, where only a small percentage of the total surface area is contributed by the edges.

To test the aforementioned dependences of the shell's crystal phase on the shape and size of the template, we synthesized Pd cubic nanocrystals with edge lengths of 6, 10, 18, and 25 nm, as well as Pd octahedral nanocrystals with edge

lengths of 14, 20, and 26 nm. 28-30 The templates were subsequently used for the deposition of Ru overlayers to give Pd@Ru core-shell nanocrystals with either a cubic or an octahedral shape. 17 We did not explore Pd nanocrystals with sizes larger than 26 nm in our study because the surface diffusion of adatoms might become an issue for the formation of a conformal shell, while the resultant nanocrystals would be outside the size range relevant for catalytic applications. Figure 1A-D shows TEM images of the Pd@Ru nanocrystals with a cubic shape, while Figure 1E-H shows the products after the Pd core had been selectively etched away using aqueous FeCl₃ to give well-defined cubic nanocages. The final structures are expected to be nanocages rather than nanoframes because the Ru shell could be made thick enough to prevent the Pd core from being etched away.³² It is also worth noting that the sample with a thicker shell still showed a relatively smooth surface, in contrast to the concave structures observed in the formation of nanoframes with a thicker ridge. 33 Figure 2 shows TEM images of similar products obtained using Pd octahedral

templates with different sizes. Both core-shell nanocrystals and nanocages were characterized by a well-defined octahedral shape, together with a smooth surface.

Next, we analyzed the as-obtained Pd@Ru nanocrystals using XRD to determine the crystal phase taken by the deposited Ru. Figure 3 shows XRD patterns of the Pd@Ru

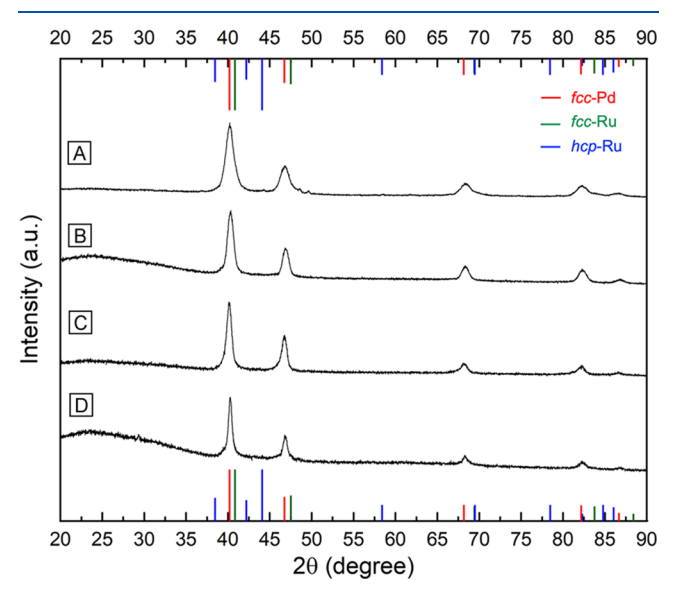


Figure 3. XRD patterns of the Pd@Ru nanocrystals derived from (A) 6-nm, (B) 10-nm, (C) 18-nm, and (D) 25-nm cubic templates, indicating the formation of fcc-Ru overlayers for all of the samples. Red, green, and blue lines correspond to the characteristic peaks of fcc-Pd (JCPDS No. 05-0685), fcc-Ru (JCPDS No. 01-088-2333), and hcp-Ru (JCPDS No. 06-0663).

cubic nanocrystals, indicating that the Ru shells took an fcc structure regardless of the template size. 12,17 In all cases, the main XRD peak was located around 40.2°, which is between the reference peaks of fcc-Pd and fcc-Ru. For core-shell nanocrystals, we do not expect to observe separate XRD peaks with strong intensities for the core and the shell. 8,20,26,34 Especially in the case where Pd and Ru adopt the same crystal phase, the observed peaks should be an average of the peaks corresponding to the core and the shell, with relative contributions depending on the shell thickness, particle size, and orientation. 8,34 In contrast, a minor separation, expressed by the presence of secondary peaks or small shoulders next to the main peaks, is expected when the core and the shell have different crystal structures. This shoulder peak arising from the core tended to vary in intensity depending on the thickness and crystal phase of the shell, the particle size, and the overall contribution of each phase to the entire sample. 20,26,27 As such. we consider the position of the main peak with the strongest intensity as the most important feature to identify the phase of the shell. In the case of Pd@Ru cubic nanocrystals with a relatively thin Ru shell, the main XRD peak around 40.2° could be assigned to an average of the fcc-Pd(111) peak at 40.1° and the fcc-Ru(111) peak at 40.7° because of the similarity in crystal structure between the core and shell. Additionally, all peaks were shifted to smaller angles compared to the reference peaks of fcc-Ru due to the tensile strain in the Ru{100} overlayers deposited on Pd{100} facets.³⁵ Notably, the lack of a well-resolved peak corresponding to the hcp-Ru phase indicates that the Ru shells were entirely composed of fcc-Ru. 8,20 Taken together, it can be concluded that the inherent

mismatch between the {100} facets of the fcc lattice and the facets of an hcp lattice forces the Ru overlayers on cubic templates into the metastable fcc phase.2

Unlike the case of cubic templates, we observed a size dependence when analyzing the Pd@Ru octahedral nanocrystals using XRD. For the 14-nm Pd@Ru octahedra, the XRD pattern in Figure 4A is similar to those obtained from the cubic

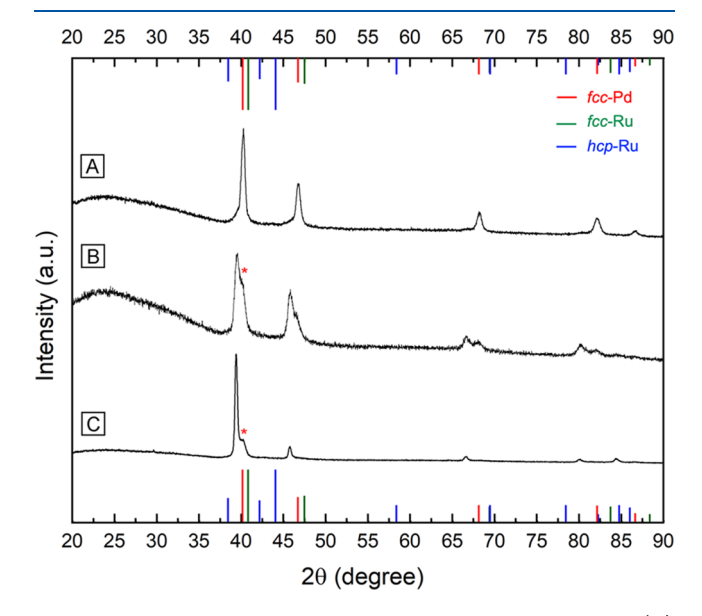


Figure 4. XRD patterns of the Pd@Ru nanocrystals derived from (A) 14-nm, (B) 20-nm, and (C) 26-nm Pd octahedral templates, indicating an fcc structure for the 14-nm particles, and an hcp structure for the 20- and 26-nm ones. Red, green, and blue lines correspond to the characteristic peaks of fcc-Pd (JCPDS No. 05-0685), fcc-Ru (JCPDS No. 01-088-2333), and hcp-Ru (JCPDS No. 06-0663). The (*) symbol in (B) and (C) denotes the shoulder peak indexed to fcc-Pd(111) plane in the octahedral nanocrystals composed of fcc-Pd core and hcp-Ru shell.

counterparts. Specifically, the appearance of a main peak at 40.2° and the lack of any secondary peaks or shoulders indicate that the Ru shells took the metastable fcc phase when deposited on the 14-nm octahedral templates.²² However, as shown in Figure 4B,C for the 20- and 26-nm Pd@Ru octahedral nanocrystals, the main peak shifted to 39.4°, in between the reference peaks of fcc-Pd and hcp-Ru, as a result of averaging between the fcc-Pd(111) peak at 40.1° and the hcp-Ru(1010) peak at 38.4°. In this case, the fcc-Pd peak at a much larger angle than that of hcp-Ru(1010) peak is responsible for shifting the observed peak to a larger angle relative to the hcp-Ru reference. In addition, a distinct shoulder peak was observed near 40.2°, which could be indexed to the (111) diffraction from fcc-Pd in the core. Variation in the intensity of this shoulder peak arising from the fcc-Pd core could be attributed to the differences in thickness and crystal phase of the Ru shell, the particle size, and the overall contribution of each phase to the entire sample. 20,26,27 These results are consistent with the argument that the XRD peaks from Pd@Ru nanocrystals with different phases in the core and shell would show a small separation between the main peaks because of the heterogeneous phases existing in one particle. It should be pointed out that shape-controlled nanocrystals often give a diffraction pattern with peaks different in relative intensities compared with that from a bulk powder sample due to the texture effect arising from the

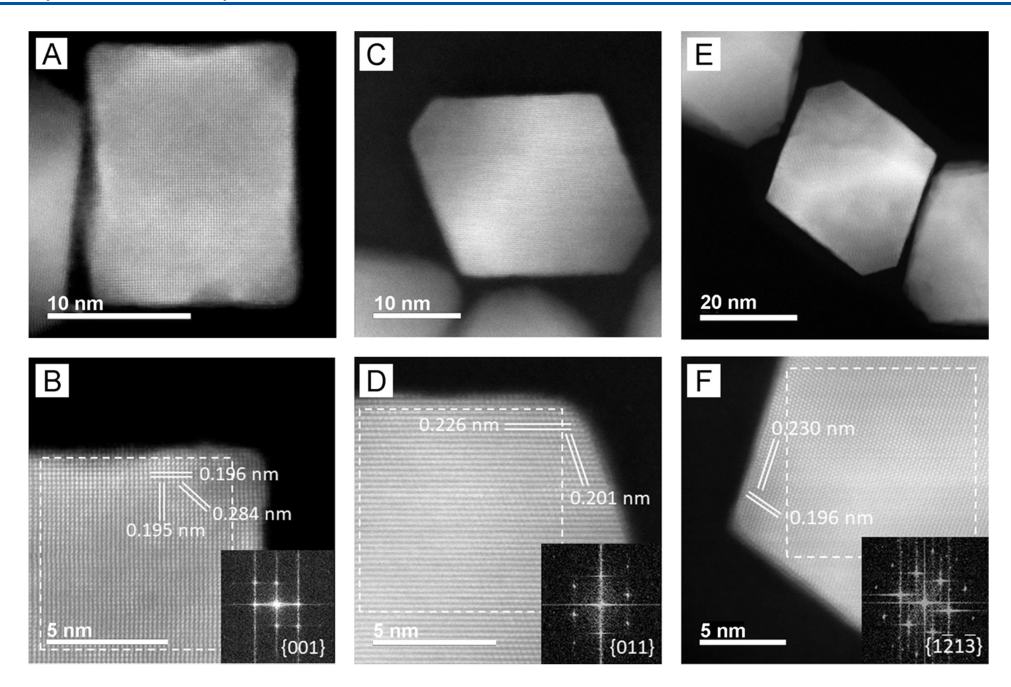


Figure 5. HAADF-STEM images of the (A, B) 18-nm Pd@Ru cubic nanocrystal and (C, D) 14-nm and (E, F) 26-nm Pd@Ru octahedral nanocrystals, respectively. The FFT patterns (inset) were obtained from the areas marked by the white boxes.

preferred orientation of nanocrystals.³⁴ From the difference in XRD pattern, it can be concluded that the Ru shell adopts the native hcp phase on the 20- and 26-nm Pd octahedral templates. There is a clear trend for the template size in affecting Ru deposition on octahedral Pd nanocrystals, with small ones resulting in the formation of fcc-Ru shell while larger ones give hcp-Ru shell. The observed dependence of crystal phase on both particle shape and size can be rationalized by the symmetry match between the facets of these two systems that allows for the deposition of either hcp-or fcc-Ru on {111} facets, with the outcome determined by the balance between bulk and surface energies as a function of particle size. ^{26,27,31}

To support the XRD data, we analyzed the 18-nm cubic, 14nm octahedral, and 26-nm octahedral Pd@Ru nanocrystals using HAADF-STEM. Fast Fourier transform (FFT) analysis of the HAADF-STEM images in Figure 5A,B indicates an fcc phase for the shell on the 18-nm Pd@Ru cubic nanocrystal, and the fringe spacings of 0.196 and 0.284 nm can be assigned to the {200} and {110} planes, respectively, of fcc-Ru. Similarly, FFT analysis of the 14-nm Pd@Ru octahedral nanocrystal in Figure 5C,D confirmed an fcc phase, with the fringe spacings of 0.226 and 0.201 nm corresponding to strained fcc-Ru {111} and {200} lattice planes, respectively. Finally, the HAADF-STEM images in Figure 5E,F show that the FFT of the 26-nm Pd@Ru octahedral nanocrystal was indicative of hcp-Ru shell, with the fringe spacings of 0.230 and 0.196 nm corresponding to strained $\{10\overline{1}0\}$ and $\{10\overline{1}1\}$ planes, respectively. Obviously, both the size and shape of the template play essential roles in determining the crystal phase of the metal deposited through templated-directed growth.

As reported in previous studies, the crystal phase of the Ru overlayers did not change when the Pd template was selectively removed by wet etching to form Ru nanocages. ^{17,21–24} Here we also confirmed the retention of the crystal structure through XRD analysis (Figure S2). The fcc, fcc, and hcp structures were maintained by the resultant Ru nanocages

when the Pd core was selectively removed from the 18-nm cubic, 14-nm octahedral, and 26-nm octahedral Pd@Ru nanocrystals, respectively, by wet etching. The slight discrepancy between the experimental and reference XRD patterns could be ascribed to the residual Pd (ca. 6%) remaining in the Ru lattice because of interdiffusion and alloying at the interface. Taken together, these results confirmed that the crystal structure of the Ru shell was robust enough to remain intact during the removal of the Pd template by wet etching.

In general, successful phase control during template-directed growth is dependent on the achievement of layer-by-layer growth mode, where the atomic diffusion rate is faster than the deposition rate.^{9,36} The island growth mode, in contrast, tends to favor the formation of the thermodynamically stable phase.²⁰ Depending on the experimental conditions, two types of island growth can result in the formation of Ru shell in its native hcp structure: epitaxial growth through heterogeneous nucleation and nonepitaxial growth through selfnucleation. In the first case, Ru atoms nucleate on the Pd surface, followed by the continuous surface reduction and deposition of Ru atoms to generate hcp-Ru islands. Alternatively, the Ru atoms nucleate in the solution and further evolve into small hcp-Ru particles, which are then loosely attached to the Pd surface. In this case, the final products tended to contain a second population of Ru particles much smaller than the original seeds. To ensure that the observed changes in the crystal phase were caused by the shape and size of the template, we examined various synthetic parameters that can affect the growth mode, including injection rate, reaction temperature, and shell thickness. 16 First, to keep the precursor concentration low enough to promote layer-bylayer growth, its injection rate had to be sufficiently slow.^{6,36} At the standard injection rate of 0.5 mL/h, layer-by-layer growth occurred to give fcc-Ru overlayers on the 18-nm cubic templates, as demonstrated in Figure 3A. As shown in Figure S3, however, if the injection rate was increased to 2 mL/h and

4 mL/h or one-shot injection was involved, hcp-Ru shell would be formed on the cubic template due to the primary involvement of nonepitaxial island growth. This trend was attested by the shift of the main peaks to the angles between the fcc-Pd(111) and hcp-Ru(1010) peaks, coupled with the presence of small shoulders with different intensities. The same effect of injection rate was also observed in the case of 14-nm octahedral template where hcp-Ru started to form on the {111} planes of fcc-Ru if the injection rate was increased, as shown in Figures 4A and S4. In both cases, the presence of smaller, quasi-spherical particles in the same sample as a byproduct suggested the dominance of nonepitaxial island growth due to self-nucleation when a fast deposition was used regardless of the shape of the templates.

Additionally, the reaction temperature was essential to ensure sufficient deposition of Ru on both the 14-nm octahedral and 18-nm cubic seeds. When the reaction temperature was decreased from the standard 180-150 °C (Figure S5A–D), no Ru was deposited, as indicated by the lack of nanocages after Pd etching as a result of the weak reducing power of EG at this temperature and insufficient reduction of the precursor.^{37,38} At 165 °C, as shown in Figure S5E-D, deposition occurred, but the Ru surfaces on both the coreshell particles and nanocages appeared to be rough due to the suppression of surface diffusion, switching the deposition mode to island growth. Meanwhile, the wall thickness of the nanocages was reduced due to inadequate reduction of the Ru precursor. When the temperature was increased to 195 °C, no changes to the deposition were observed, as both diffusion and deposition remained adequately fast, as seen in Figure S5I-L.³⁶ Altogether, a sufficiently high temperature is the prerequisite to not only ensure an adequate reducing power and thus an enough supply of Ru atoms, but also maintain a favorable surface diffusion over atom deposition for generating a conformal shell.

Finally, to allow for phase control, the shell thickness had to be kept below ca. 5 atomic layers. ^{17,39} Figure S6A,B,D,E shows that with a thin shell, metastable fcc-Ru was formed on the 18nm cubic template. When the shell became thicker, Ru reverted to the hcp phase, as seen in Figure S6C,F. In this case, the increased concentration of Ru(III) precursor in each droplet caused a shift to nonepitaxial island growth as a result of faster reduction kinetics and thus self-nucleation. This growth mode is evident by the presence of individual particles loosely attached to the surface of the cubic template. For 14nm Pd@Ru octahedral nanocrystals, the same trend associated with the increase in shell thickness is documented in Figure S7. Overall, when the requirements for faster diffusion over deposition rates are not met, epitaxial island growth or nonepitaxial growth due to self-nucleation could transpire individually or simultaneously to hinder the conformal deposition and thus the creation of Ru overlayers in its native hcp structure. Notably, in the case involving cubic templates, hcp-Ru should be exclusively formed via self-nucleation and then loosely attached to the surface of Pd template rather than epitaxially grown from the template, as the symmetry mismatch with the fcc-{100} facets would make the overgrowth of smooth hcp shell on the cubic templates difficult. $^{11,2\delta}$ When all of these parameters for Ru deposition were optimized to achieve layer-by-layer growth (i.e., 0.5 mL/h injection rate, thin shells, and 180 °C), we were able to control the phase taken by the deposited Ru. The TEM images in Figures S8 and S9 confirm that no deposition of particles arising from selfnucleation, or other indicators of epitaxial island growth (*i.e.*, rough surface), was observed at any point during the synthesis involving either 18-nm cubic or 14-nm octahedral templates. It is worth emphasizing that these optimal parameters were used to prepare all of the samples reported in this work that involved layer-by-layer growth to ensure that the observed changes in crystal phase were caused by the shape and size of the template.

The aforementioned parameters vital to achieving layer-bylayer growth have been reported previously. 11,16,31 However, during this study, it became apparent that water also played a crucial role in controlling the phase taken by the Ru shell. To our knowledge, this factor has not been reported in the literature. The template-directed Ru deposition is conducted in EG while the Pd templates are synthesized in water. Prior to their use, the templates were collected and then redispersed in EG, but even with the utmost care, a few microliters of water were always trapped in the templates. For this reason, we heated the reaction solution (after the introduction of templates) for at least 30 min at 180 °C to evaporate the residual water. If the evaporation period was shortened, the Ru shell displayed an hcp phase, even if all other parameters were favorable for layer-by-layer growth. To test the effects of water on the resultant crystal phase, water was added in different ways. When depositing Ru on the 18-nm Pd cubic seeds, it was only possible to get fcc-Ru when the templates were collected and then dispersed in EG, and the reaction was preheated to remove any residual water, as shown in Figure 6A. In contrast, as shown in Figure 6B,E,C,F, if water was added into either the Ru(III) precursor solution or the reaction vial containing Pd templates, the as-obtained Ru shell was relatively rough and always in the hcp phase. Similarly, as shown in Figure 6D,G, if the templates were dispersed in water instead of EG, the Ru shell also took an hcp phase. It should be noted that the weaker intensity of the shoulder peak corresponding to the Pd core in Figure 6D,G could be attributed to the larger number of small hcp-Ru nanoparticles formed due to self-nucleation, thus leading to a stronger contribution of hcp phase to the XRD patterns relative to those in Figure 6B,E,C,F. Figure 7 shows the same effect of water on the crystal structure taken by the Ru particles attached to the surface of the 14-nm Pd octahedral template.

The detrimental effect of water on phase-controlled deposition could be ascribed to its ability to speed up the reduction kinetics of the Ru(III) precursor. 40,41 Water has been shown to increase the electron transfer in an EG-based synthesis by increasing the polarity of the system, thereby speeding up the reduction of a metal precursor. 41-43 In another study, the addition of only a small amount of water to a polyol system was shown to act as a catalyst to speed up the reduction of metal chlorides. 40 The water can coordinate with the metal ion, thereby inducing a reaction pathway where several intermediate steps have lower activation energies compared to the water-free pathway. The lower activation energies result in faster reaction rates for those steps and an overall faster reduction rate of the precursor. As shown by the TEM images in Figures 6 and 7, there are small particles present in the samples with added water, which are likely formed through self-nucleation. Careful examination of the HADAAF-STEM image of the core-shell nanocrystals prepared by adding water into the Ru(III) precursor solution reveals the interface between the Pd cubic template and the rough Ru shell, suggesting that the shell was composed of hcp-

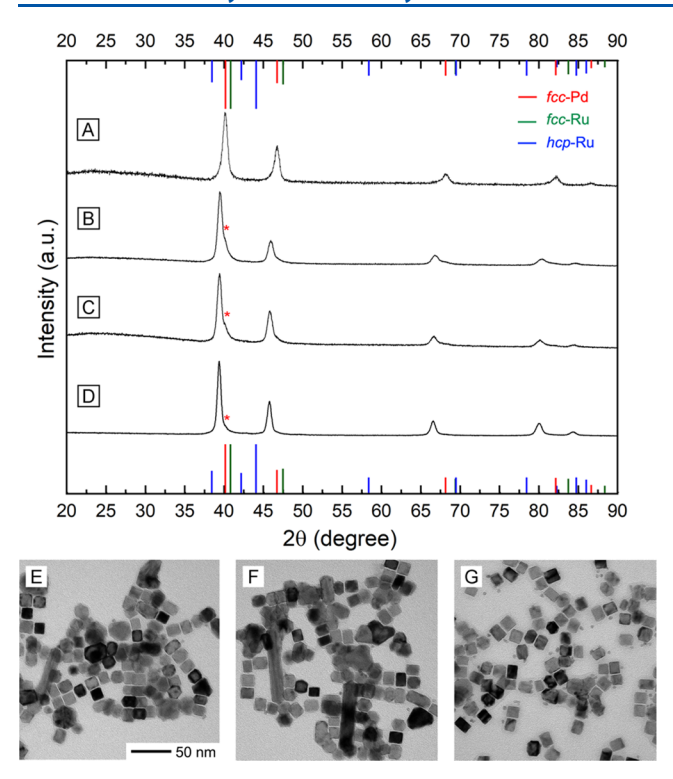


Figure 6. (A-D) XRD patterns and (E-G) TEM images of the Pd@ Ru nanocrystals derived from 18-nm Pd cubic templates with or without the influence of water. (A) The templates were dispersed in EG in the absence of additional water and preheated for 30 min (standard protocol, see TEM image in Figure 1C), (B, E) The templates were dispersed in EG while the precursor was dissolved in the water/EG mixture (1:1 v/v). (C, F) The templates were redispersed in EG with additional water introduced into the reaction vial, and (D, G) the templates dispersed in water in the absence of additional water in either precursor or growth solution. Note that no preheating to remove water was carried out in the control experiments in (B)-(G). Red, green, and blue lines correspond to the characteristic peaks of fcc-Pd, fcc-Ru, and hcp-Ru. The (*) symbol in (B)–(D) denotes the shoulder peak indexed to fcc-Pd(111) plane in the cubic nanocrystals composed of fcc-Pd core and hcp-Ru shell. The scale bar in (E) applies to all panels.

Ru particles loosely attached to the template's surface (Figure S10). In this case, hcp-Ru particles would be formed *via* self-nucleation and then attached to the edges and side faces of the templates. While self-nucleation would use up some of the available Ru precursor, the small size and quantity of those secondary particles mean that we do not expect that the XRD pattern or shell thickness would be strongly affected. Taken together, the introduction of water would speed up the reduction of the Ru(III) precursor, thereby impeding template-directed phase control. The nonepitaxial growth mode activated by the accelerated reduction kinetics presents an alternative route to override the symmetry mismatch between fcc-{100} and any hcp facets, thereby inducing the formation of hcp-Ru shell on the Pd cubic template.

Finally, we evaluated and compared the catalytic properties of the phase-controlled Pd@Ru nanocrystals toward EGOR, a reaction responsible for the operation of direct ethylene glycol fuel cells. The Pd@Ru nanocrystals, as well as the hcp-Ru nanoparticles serving as a reference, were deposited on a carbon support at a total metal loading of *ca.* 20 wt %. The Ru nanoparticles had a small size of 3.5 nm, a quasi-spherical shape, and a native hcp structure as confirmed by TEM and

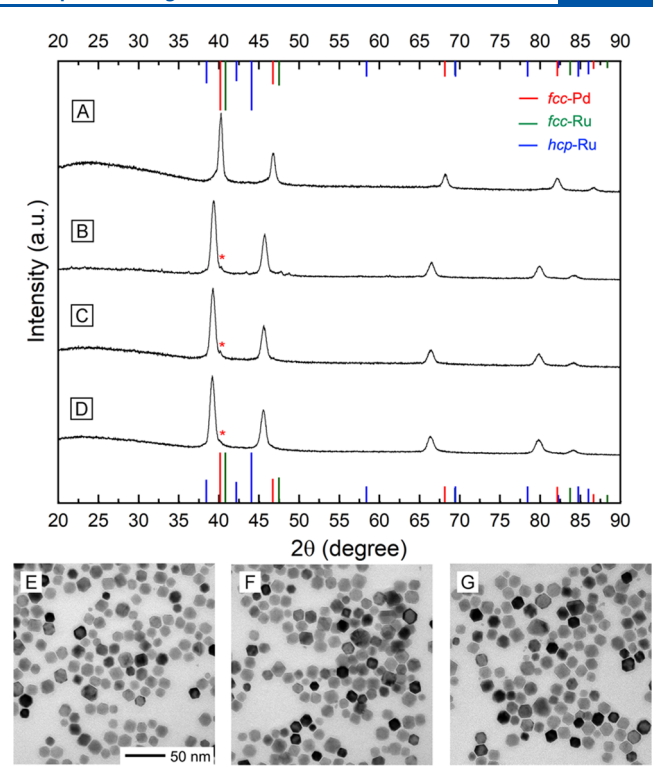
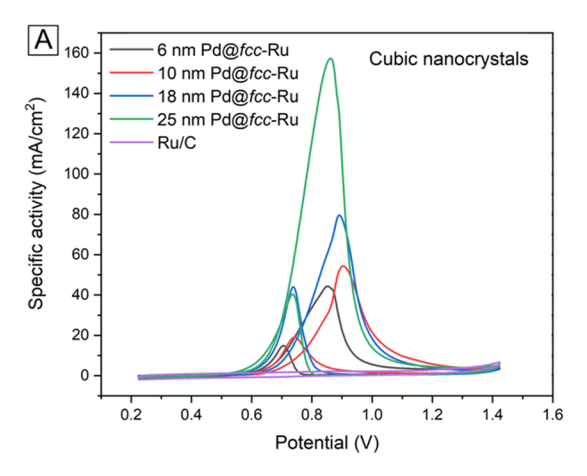


Figure 7. (A-D) XRD patterns and (E-G) TEM images of the Pd@ Ru nanocrystals derived from the 14-nm Pd octahedral templates with or without the influence of water. (A) The templates were dispersed in EG in the absence of additional water and preheated for 30 min (standard protocol, see the TEM image in Figure 2A). (B, E) The templates were dispersed in EG while the precursor was dissolved in the water/EG mixture (1:1 v/v). (C, F) The templates were dispersed in EG with additional water introduced into the reaction vial. (D, G) The templates were dispersed in water in the absence of additional water in either precursor or growth solution. Note that no preheating to remove water was carried out in the control experiments in (B)-(G). Red, blue, and green lines correspond to the characteristic peaks of fcc-Pd, hcp-Ru, and fcc-Ru. The (*) symbol in (B)-(D) denotes the shoulder peak indexed to fcc-Pd(111) plane in the octahedral nanocrystals composed of fcc-Pd core and hcp-Ru shell. The scale bar in (E) applies to all panels.

XRD analyses (Figure S11). We controlled the shell thicknesses of the Pd@Ru nanocrystals to ensure that the difference in catalytic activity was not caused by the variation in the Ru thickness. Specifically, the shell thicknesses were 1.00, 1.02, 0.93, 0.89 nm for the 6-, 10-, 18-, and 25-nm cubic nanocrystals, and respectively, and 0.95, 0.99, and 1.06 nm for the 14-, 20-, and 26-nm octahedral nanocrystals, respectively. The surface of all of the Pd@Ru core—shell particles should be mainly covered by Ru. A small amount of Pd might be exposed on the outer surface as a result of interdiffusion into the Ru shell and/or presence of pinholes in the Ru shell. However, since all the reported samples had a similar shell thickness, the contribution from any exposed Pd should be more or less on the same level. 17,22,23,31 Altogether, the conclusions drawn below regarding the effects of shape, size, and crystal phase on the catalytic activity should not be affected by the possible involvement of Pd exposure on the surface.

The cyclic voltammetry (CV) curves of the as-obtained catalysts are shown in Figure 8, with the hcp-Ru nanoparticles displaying negligible activity compared to either cubic or octahedral Pd@Ru nanocrystals. Monometallic Ru is known to



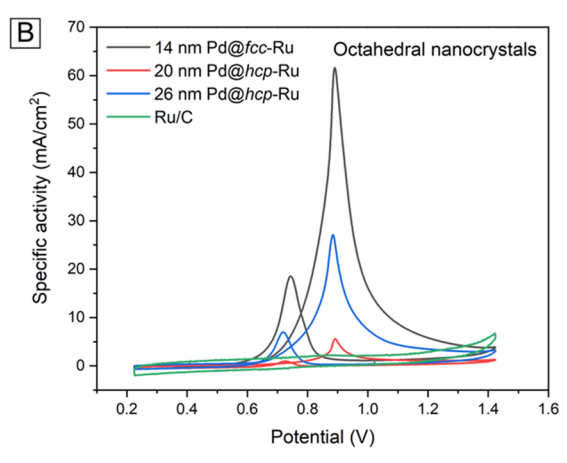


Figure 8. (A) CV curves for EGOR on the Pd@Ru nanocrystals derived from 6-, 10-, 18-, and 25-nm cubic templates and hcp-Ru/C, recorded in an Ar-saturated solution containing 1.0 M KOH and 1.0 M EG. The current density was normalized to the corresponding ECSA. (B) CV curves for EGOR on the Pd@Ru nanocrystals derived from 14-, 20-, and 26-nm octahedral templates and hcp-Ru/C, recorded in an Ar-saturated solution containing 1.0 M KOH and 1.0 M EG.

be a poor catalyst toward EGOR. In contrast, Pd is a good catalyst toward EGOR, albeit CO poisoning generally causes almost immediate deactivation of the catalyst. 44,45 As a result, the interaction between the Pd core and the Ru shell should be responsible for the much-improved activity of the core-shell particles relative to hcp-Ru. First of all, oxygen species can easily bind to Ru surfaces, helping remove the poisoning CO and thereby keeping the catalyst active. 45,46 Second, Pd and Ru can have beneficial electronic effects when arranged in a coreshell configuration to improve charge transfer and thus weaken CO binding to the surface, improving catalytic activity while mitigating the poisoning effect. 44,47-49 Finally, the strain and ligand effects between Pd and Ru facilitate the breaking of C-C bonds during alcohol oxidation, an essential step in the overall reaction that helps promote a more complete oxidation of EG. 44,45,50,51 Altogether, the Pd in the core is able to modulate the electronic structure of the Ru shell, activating it toward EGOR.

The Pd@Ru cubic nanocrystals outperformed the octahedral counterparts of a similar size, with the trend being attributed to the difference in surface atomic arrangement, as caused by the variation in crystal phase and/or particle shape. For the 25-nm Pd@fcc-Ru cubic particles and the 26-nm Pd@hcp-Ru octahedral particles, their peak-specific activities differ almost 5-fold (147.3 versus 26.6 mA/cm²). This result is likely due to the different facets on the cubic and octahedral particles as a result of the variations in crystal phase and particle shape. Previous studies have shown that {100} facets were more active than the {111} facets toward alcohol oxidation, as the breaking of the C-C bond is promoted by a stronger binding of the alcohol to the less closely packed {100} facets. Since both the fcc-{111} and hcp-{0001} facets have the same C₃ arrangement for the surface atoms, this trend should still hold. Additionally, the 18-nm cubic and 14-nm octahedral Pd@fcc-Ru particles also showed a difference in peak activity: 78.8 versus 60.7 mA/cm². Again, when crystallized in the same fcc lattice, the {100} facets on cubic particles outperformed the {111} facets on octahedral counterparts due to the stronger binding of alcohol to {100} facets. 52,53 To this end, shape control remains important in affecting catalytic activity.

In addition to the geometric shape, the crystal phase and size of nanocrystals can also impact the catalytic activity. For the Pd@Ru cubic nanocrystals, they all had an fcc-Ru shell, but

their specific activity increased as the particles became larger (Figure 8A). In general, as nanocrystals become smaller in size, the proportion of atoms situated at the edges and corners will increase, while the proportion of atoms on the side faces will decrease. 54 Since the {100} facets on the side faces of a cubic nanocrystal are more active toward EGOR than the {110} and {111} facets exposed on the edges and corners, the increased proportion of {100} facets on the larger cubic nanocrystals is expected to increase the area-specific catalytic activity. 45,55 For the octahedral nanocrystals, the 26- and 20-nm Pd@hcp-Ru samples show the same direct correlation between size and activity (26.6 and 5.6 mA/cm², respectively) as observed for the cubic samples, but the smallest 14-nm Pd@fcc-Ru particles exhibited the highest specific activity at 60.7 mA/cm² (Figure 8B). The main difference between the 14-nm octahedral nanocrystals and the 26- or 20-nm counterparts was the crystal phase, and this difference should be responsible for the improved activity toward EGOR. First, the tensile strain experienced by the fcc-Ru can help promote the C-C bond breaking for the generation of C₂ rather than C₁ products, thereby favoring more complete EG oxidation. ⁵¹ Next, as mentioned before, CO is a poisoning species for EGOR, 44,53 and fcc-Ru has been shown to be a better catalyst toward CO oxidation, and thus less prone to CO poisoning than hcp-Ru. 12 Altogether, we believe that the improved catalytic activity of the Pd@fcc-Ru nanocrystals can be attributed to more complete oxidation and thus a larger number of available active sites compared to the Pd@hcp-Ru counterparts.

We also characterized the core—shell nanocrystals after the electrochemical test. Figure S12 shows the HAADF-STEM image recorded from one of the 18-nm Pd@Ru cubic nanocrystals after they had gone through the electrochemical measurement in Figure 8A. Although the side faces of the nanocrystal became slightly concave due to the possible dissolution of Pd, our analyses of the FFT pattern and the lattice fringe spacing before and after EGOR confirmed that the Ru shell remained in the metastable fcc phase despite the electrochemical processes involved. We expect that the crystal phase of the Ru shell should be retained during electrochemical tests for all other Pd@Ru core—shell nanocrystals as well. Once the crystal structure has been fixed, one only needs to optimize the shape and size of the catalytic particles when developing the most effective catalyst toward EGOR.

CONCLUSIONS

We have systematically investigated the crystal phase taken by Ru atoms upon deposition on Pd cubic and octahedral nanocrystals with different sizes. Our results indicate that the size of the Pd nanocrystal template can affect the crystal phase by altering the balance between bulk and surface energies, while the shape of the template plays a role through the symmetry alignment between different facets. Specifically, when Ru is deposited on Pd cubic templates of 6-25 nm in size, it always takes an fcc phase as no facet in the hcp structure can align with the fcc-{100} facets. In contrast, the deposited Ru takes an fcc phase on 14-nm Pd octahedral template but reverts to the stable hcp phase on both 20- and 26-nm octahedral templates. Because of the symmetry alignment between the fcc-{111} and hcp-{0001} facets, Ru atoms can take either an fcc or hcp phase when deposited on the {111} facets of an octahedral template. The dependence of phase on template size can be attributed to a shift in balance between the surface and bulk energies as the area proportions of edges and faces on the octahedral template change. Additionally, the presence of water in the reaction complicates phase control, as it speeds up the reaction kinetics to induce nonepitaxial growth and thus the formation of a rough shell composed of loosely attached hcp-Ru islands. When the Pd@Ru nanocrystals are evaluated as catalysts toward EGOR, the fcc-Ru outperforms the hcp-Ru, as reflected by the superior activity of cubic particles over the octahedral counterparts. Altogether, this study has demonstrated the importance of particle shape and size in the template-directed synthesis of nanocrystals with different phases, moving toward an ultimate control over the polymorphism of noble metals.

ASSOCIATED CONTENT

Supporting Information

The Supporting Information is available free of charge at https://pubs.acs.org/doi/10.1021/acs.jpcc.2c08825.

Additional XRD patterns, as well as TEM and HAADF-STEM images of the samples prepared under different conditions and collected after electrochemical measurements, helping elucidate the mechanistic details of the synthesis and the stability of the metastable phase (PDF)

AUTHOR INFORMATION

Corresponding Author

Younan Xia — School of Chemistry and Biochemistry, Georgia Institute of Technology, Atlanta, Georgia 30332, United States; The Wallace H. Coulter Department of Biomedical Engineering, Georgia Institute of Technology and Emory University, Atlanta, Georgia 30332, United States; orcid.org/0000-0003-2431-7048; Email: younan.xia@bme.gatech.edu

Authors

Annemieke Janssen — School of Chemistry and Biochemistry, Georgia Institute of Technology, Atlanta, Georgia 30332, United States; ocid.org/0000-0002-7721-597X

Quynh N. Nguyen – School of Chemistry and Biochemistry, Georgia Institute of Technology, Atlanta, Georgia 30332, United States; Oorcid.org/0000-0003-1544-6139

- Zhiheng Lyu School of Chemistry and Biochemistry, Georgia Institute of Technology, Atlanta, Georgia 30332, United States; o orcid.org/0000-0002-1343-4057
- Veronica Pawlik School of Chemistry and Biochemistry, Georgia Institute of Technology, Atlanta, Georgia 30332, United States
- Chenxiao Wang School of Chemistry and Biochemistry, Georgia Institute of Technology, Atlanta, Georgia 30332, United States

Complete contact information is available at: https://pubs.acs.org/10.1021/acs.jpcc.2c08825

Author Contributions

§A.J. and Q.N.N. contributed equally to this work.

Notes

The authors declare no competing financial interest.

ACKNOWLEDGMENTS

This work was supported in part by a grant from the National Science Foundation (CHE 2105602) and start-up funds from the Georgia Institute of Technology. Q.N.N. acknowledges the support from the National Science Foundation Graduate Research Fellowship under Grant No. DGE-2039655. TEM imaging was performed in part at the Georgia Tech Institute for Electronics and Nanotechnology, a member of the National Nanotechnology Coordinated Infrastructure (NNCI), which is supported by the National Science Foundation (ECCS-2025462).

REFERENCES

- (1) Quinson, J.; Jensen, K. M. Ø. From Platinum Atoms in Molecules to Colloidal Nanoparticles: A Review on Reduction, Nucleation and Growth Mechanisms. *Adv. Colloid Interface Sci.* **2020**, 286, No. 102300.
- (2) Elechiguerra, J. L.; Reyes-Gasga, J.; Yacaman, M. J. The Role of Twinning in Shape Evolution of Anisotropic Noble Metal Nanostructures. *J. Mater. Chem.* **2006**, *16*, 3906–3919.
- (3) Liu, X.; Luo, J.; Zhu, J. Size Effect on the Crystal Structure of Silver Nanowires. *Nano Lett.* **2006**, *6*, 408–412.
- (4) Skrabalak, S. E. Symmetry in Seeded Metal Nanocrystal Growth. *Acc. Mater. Res.* **2021**, *2*, 621–629.
- (5) Chen, Z.; Balankura, T.; Fichthorn, K. A.; Rioux, R. M. Revisiting the Polyol Synthesis of Silver Nanostructures: Role of Chloride in Nanocube Formation. *ACS Nano* **2019**, *13*, 1849–1860.
- (6) Zhang, H.; Li, W.; Jin, M.; Zeng, J.; Yu, T.; Yang, D.; Xia, Y. Controlling the Morphology of Rhodium Nanocrystals by Manipulating the Growth Kinetics with a Syringe Pump. *Nano Lett.* **2011**, *11*, 898–903.
- (7) Yang, T. H.; Gilroy, K. D.; Xia, Y. Reduction Rate as a Quantitative Knob for Achieving Deterministic Synthesis of Colloidal Metal Nanocrystals. *Chem. Sci.* **2017**, *8*, 6730–6749.
- (8) Rostek, A.; Loza, K.; Heggen, M.; Epple, M. X-ray Powder Diffraction to Analyse Bimetallic Core—Shell Nanoparticles (Gold and Palladium; 7–8 nm). RSC Adv. 2019, 9, 15373–15380.
- (9) Xia, Y.; Gilroy, K. D.; Peng, H. C.; Xia, X. Seed-Mediated Growth of Colloidal Metal Nanocrystals. *Angew. Chem., Int. Ed.* **2017**, *56*, 60–95.
- (10) Cheng, H.; Yang, N.; Lu, Q.; Zhang, Z.; Zhang, H. Syntheses and Properties of Metal Nanomaterials with Novel Crystal Phases. *Adv. Mater.* **2018**, *30*, No. e1707189.
- (11) Janssen, A.; Nguyen, Q. N.; Xia, Y. Colloidal Metal Nanocrystals with Metastable Crystal Structures. *Angew. Chem., Int. Ed.* **2021**, *60*, 12192–12203.
- (12) Kusada, K.; Kobayashi, H.; Yamamoto, T.; Matsumura, S.; Sumi, N.; Sato, K.; Nagaoka, K.; Kubota, Y.; Kitagawa, H. Discovery

- of Face-Centered-Cubic Ruthenium Nanoparticles: Facile Size-Controlled Synthesis Using the Chemical Reduction Method. *J. Am. Chem. Soc.* **2013**, *135*, 5493–5496.
- (13) Huang, X.; Li, S.; Huang, Y.; Wu, S.; Zhou, X.; Li, S.; Gan, C. L.; Boey, F.; Mirkin, C. A.; Zhang, H. Synthesis of Hexagonal Close-Packed Gold Nanostructures. *Nat. Commun.* **2011**, *2*, No. 292.
- (14) Kusada, K.; Kitagawa, H. A Route for Phase Control in Metal Nanoparticles: A Potential Strategy to Create Advanced Materials. *Adv. Mater.* **2016**, 28, 1129–1142.
- (15) Huang, J. L.; Li, Z.; Duan, H. H.; Cheng, Z. Y.; Li, Y. D.; Zhu, J.; Yu, R. Formation of Hexagonal-Close Packed (HCP) Rhodium as a Size Effect. *J. Am. Chem. Soc.* **2017**, *139*, 575–578.
- (16) Fan, Z.; Zhang, H. Template Synthesis of Noble Metal Nanocrystals with Unusual Crystal Structures and Their Catalytic Applications. *Acc. Chem. Res.* **2016**, *49*, 2841–2850.
- (17) Zhao, M.; Figueroa-Cosme, L.; Elnabawy, A. O.; Vara, M.; Yang, X.; Roling, L. T.; Chi, M.; Mavrikakis, M.; Xia, Y. Synthesis and Characterization of Ru Cubic Nanocages with a Face-Centered Cubic Structure by Templating with Pd Nanocubes. *Nano Lett.* **2016**, *16*, 5310–5317.
- (18) Fan, Z.; Chen, Y.; Zhu, Y.; Wang, J.; Li, B.; Zong, Y.; Han, Y.; Zhang, H. Epitaxial Growth of Unusual 4H Hexagonal Ir, Rh, Os, Ru and Cu Nanostructures on 4H Au Nanoribbons. *Chem. Sci.* **2017**, 8, 795–799
- (19) Chen, Y.; Fan, Z.; Luo, Z.; Liu, X.; Lai, Z.; Li, B.; Zong, Y.; Gu, L.; Zhang, H. High-Yield Synthesis of Crystal-Phase-Heterostructured 4H/fcc Au@Pd Core—Shell Nanorods for Electrocatalytic Ethanol Oxidation. *Adv. Mater.* **2017**, *29*, No. 1701331.
- (20) Janssen, A.; Pawlik, V.; von Rueden, A. D.; Xu, L.; Wang, C.; Mavrikakis, M.; Xia, Y. Facile Synthesis of Palladium-Based Nanocrystals with Different Crystal Phases and a Comparison of Their Catalytic Properties. *Adv. Mater.* **2021**, *33*, No. 2103801.
- (21) Ye, H.; Wang, Q.; Catalano, M.; Lu, N.; Vermeylen, J.; Kim, M. J.; Liu, Y.; Sun, Y.; Xia, X. Ru Nanoframes with an fcc Structure and Enhanced Catalytic Properties. *Nano Lett.* **2016**, *16*, 2812–2817.
- (22) Zhao, M.; Elnabawy, A. O.; Vara, M.; Xu, L.; Hood, Z. D.; Yang, X.; Gilroy, K. D.; Figueroa-Cosme, L.; Chi, M.; Mavrikakis, M.; Xia, Y. Facile Synthesis of Ru-Based Octahedral Nanocages with Ultrathin Walls in a Face-Centered Cubic Structure. *Chem. Mater.* 2017, 29, 9227–9237.
- (23) Zhao, M.; Xu, L.; Vara, M.; Elnabawy, A. O.; Gilroy, K. D.; Hood, Z. D.; Zhou, S.; Figueroa-Cosme, L.; Chi, M.; Mavrikakis, M.; Xia, Y. Synthesis of Ru Icosahedral Nanocages with a Face-Centered-Cubic Structure and Evaluation of Their Catalytic Properties. *ACS Catal.* **2018**, *8*, 6948–6960.
- (24) Zhao, M.; Hood, Z. D.; Vara, M.; Gilroy, K. D.; Chi, M.; Xia, Y. Ruthenium Nanoframes in the Face-Centered Cubic Phase: Facile Synthesis and Their Enhanced Catalytic Performance. *ACS Nano* **2019**, *13*, 7241–7251.
- (25) Zhao, M.; Chen, Z.; Lyu, Z.; Hood, Z. D.; Xie, M.; Vara, M.; Chi, M.; Xia, Y. Ru Octahedral Nanocrystals with a Face-Centered Cubic Structure, {111} Facets, Thermal Stability up to 400 °C, and Enhanced Catalytic Activity. *J. Am. Chem. Soc.* **2019**, *141*, 7028–7036.
- (26) Gu, J.; Guo, Y.; Jiang, Y.-Y.; Zhu, W.; Xu, Y.-S.; Zhao, Z.-Q.; Liu, J.-X.; Li, W.-X.; Jin, C.-H.; Yan, C.-H.; Zhang, Y. W. Robust Phase Control through Hetero-Seeded Epitaxial Growth for Face-Centered Cubic Pt@Ru Nanotetrahedrons with Superior Hydrogen Electro-Oxidation Activity. *J. Phys. Chem. C* 2015, 119, 17697—17706.
- (27) Janssen, A.; Lyu, Z.; Figueras-Valls, M.; Chao, H.-Y.; Shi, Y.; Pawlik, V.; Chi, M.; Mavrikakis, M.; Xia, Y. Phase-Controlled Synthesis of Ru Nanocrystals via Template-Directed Growth: Surface Energy versus Bulk Energy. *Nano Lett.* **2022**, *22*, 3591–3597.
- (28) Jin, M.; Liu, H.; Zhang, H.; Xie, Z.; Liu, J.; Xia, Y. Synthesis of Pd Nanocrystals Enclosed by {100} Facets and with Sizes <10 nm for Application in CO Oxidation. *Nano Res.* **2010**, *4*, 83–91.
- (29) Lai, K. C.; Chen, M.; Williams, B.; Han, Y.; Tsung, C.-K.; Huang, W.; Evans, J. W. Reshaping of Truncated Pd Nanocubes: Energetic and Kinetic Analysis Integrating Transmission Electron

- Microscopy with Atomistic-Level and Coarse-Grained Modeling. ACS Nano 2020, 14, 8551–8561.
- (30) Jin, M.; Zhang, H.; Xie, Z.; Xia, Y. Palladium Nanocrystals Enclosed by {100} and {111} Facets in Controlled Proportions and Their Catalytic Activities for Formic Acid Oxidation. *Energy Environ. Sci.* **2012**, *5*, 6352–6357.
- (31) Zhao, M.; Xia, Y. Crystal-Phase and Surface-Structure Engineering of Ruthenium Nanocrystals. *Nat. Rev. Mater.* **2020**, *5*, 440–459.
- (32) Zhao, M.; Wang, X.; Yang, X.; Gilroy, K. D.; Qin, D.; Xia, Y. Hollow Metal Nanocrystals with Ultrathin, Porous Walls and Well-Controlled Surface Structures. *Adv. Mater.* **2018**, *30*, No. e1801956.
- (33) Xie, S.; Lu, N.; Xie, Z.; Wang, J.; Kim, M. J.; Xia, Y. Synthesis of Pd-Rh Core—Frame Concave Nanocubes and Their Conversion to Rh Cubic Nanoframes by Selective Etching of the Pd Cores. *Angew. Chem., Int. Ed.* **2012**, *51*, 10266–10270.
- (34) Holder, C. F.; Schaak, R. E. Tutorial on Powder X-ray Diffraction for Characterizing Nanoscale Materials. *ACS Nano* **2019**, 13, 7359–7365.
- (35) Shriver, D.; Atkins, P. *Inorganic Chemistry*, 5th ed.; W. H. Freeman: New York, 2009; pp 223–226.
- (36) Xia, X.; Xie, S.; Liu, M.; Peng, H. C.; Lu, N.; Wang, J.; Kim, M. J.; Xia, Y. On the Role of Surface Diffusion in Determining the Shape or Morphology of Noble-Metal Nanocrystals. *Proc. Natl. Acad. Sci. U.S.A* **2013**, *110*, 6669–6673.
- (37) Rodrigues, T. S.; Zhao, M.; Yang, T. H.; Gilroy, K. D.; da Silva, A. G. M.; Camargo, P. H. C.; Xia, Y. Synthesis of Colloidal Metal Nanocrystals: A Comprehensive Review on the Reductants. *Chem. Eur. J.* **2018**, *24*, 16944–16963.
- (38) Lide, D.; Haynes, W. CRC Handbook of Chemistry and Physics, 2009–2010, 90th ed. J. Am. Chem. Soc. 2009, 131, 12862.
- (39) Sneed, B. T.; Young, A. P.; Tsung, C. K. Building Up Strain in Colloidal Metal Nanoparticle Catalysts. *Nanoscale* **2015**, *7*, 12248–12265.
- (40) Chen, S.; Yang, Q.; Wang, H.; Zhang, S.; Li, J.; Wang, Y.; Chu, W.; Ye, Q.; Song, L. Initial Reaction Mechanism of Platinum Nanoparticle in Methanol—Water System and the Anomalous Catalytic Effect of Water. *Nano Lett.* **2015**, *15*, 5961–5968.
- (41) Jia, D.; Zhao, Y.; Wei, W.; Chen, C.; Lei, G.; Wan, M.; Tao, J.; Li, S.; Ji, S.; Ye, C. Synthesis of Very Thin Ag Nanowires with Fewer Particles by Suppressing Secondary Seeding. *CrystEngComm* **2017**, *19*, 148–153
- (42) Merte, L. R.; Peng, G.; Bechstein, R.; Rieboldt, F.; Farberow, C. A.; Grabow, L. C.; Kudernatsch, W.; Wendt, S.; Lægsgaard, E.; Mavrikakis, M.; Besenbacher, F. Water-Mediated Proton Hopping on an Iron Oxide Surface. *Science* **2012**, *336*, 889–893.
- (43) Zhao, W.; Wang, S.-S.; Cao, H.-T.; Xie, L.-H.; Hong, C.-S.; Jin, L.-Z.; Yu, M.-N.; Zhang, H.; Zhang, Z.-Y.; Huang, L.-H.; Huang, W. An Eco-Friendly Water-Assisted Polyol Method to Enhance the Aspect Ratio of Silver Nanowires. *RSC Adv.* **2019**, *9*, 1933–1938.
- (44) Serov, A.; Kwak, C. Recent Achievements in Direct Ethylene Glycol Fuel Cells (DEGFC). *Appl. Catal., B* **2010**, *97*, 1–12.
- (45) Zhao, M.; Lyu, Z.; Xie, M.; Hood, Z. D.; Cao, Z.; Chi, M.; Xia, Y. Pd-Ru Alloy Nanocages with a Face-Centered Cubic Structure and Their Enhanced Activity toward the Oxidation of Ethylene Glycol and Glycerol. *Small Methods* **2020**, *4*, No. 1900843.
- (46) Xie, J.; Zhang, Q.; Gu, L.; Xu, S.; Wang, P.; Liu, J.; Ding, Y.; Yao, Y. F.; Nan, C.; Zhao, M.; et al. Ruthenium—Platinum Core—Shell Nanocatalysts with Substantially Enhanced Activity and Durability Towards Methanol Oxidation. *Nano Energy* **2016**, *21*, 247–257.
- (47) Alayoglu, S.; Nilekar, A. U.; Mavrikakis, M.; Eichhorn, B. Ru–Pt Core–Shell Nanoparticles for Preferential Oxidation of Carbon Monoxide in Hydrogen. *Nat. Mater.* **2008**, *7*, 333–338.
- (48) Kim, H. J.; Choi, S. M.; Green, S.; Tompsett, G. A.; Lee, S. H.; Huber, G. W.; Kim, W. B. Highly Active and Stable PtRuSn/C Catalyst for Electrooxidations of Ethylene Glycol and Glycerol. *Appl. Catal., B* **2011**, *101*, 366–375.

- (49) Chen, T.-Y.; Lee, G.-W.; Liu, Y.-T.; Liao, Y.-F.; Huang, C.-C.; Lin, D.-S.; Lin, T.-L. Heterojunction Confinement on the Atomic Structure Evolution of Near Monolayer Core—Shell Nanocatalysts in Redox Reactions of a Direct Methanol Fuel Cell. *J. Mater. Chem. A* **2015**, *3*, 1518—1529.
- (50) Mahata, A.; Rawat, K. S.; Choudhuri, I.; Pathak, B. Single-Layered Platinum Nanocage: a Highly Selective and Efficient Catalyst for Fuel Cells. *J. Mater. Chem. A* **2016**, *4*, 12756–12767.
- (51) Liu, M.; Xie, M.; Jiang, Y.; Liu, Z.; Lu, Y.; Zhang, S.; Zhang, Z.; Wang, X.; Liu, K.; Zhang, Q.; et al. Core—Shell Nanoparticles with Tensile Strain Enable Highly Efficient Electrochemical Ethanol Oxidation. *J. Mater. Chem. A* **2021**, *9*, 15373–15380.
- (52) Wang, H.-F.; Liu, Z.-P. Comprehensive Mechanism and Structure-Sensitivity of Ethanol Oxidation on Platinum: New Transition-State Searching Method for Resolving the Complex Reaction Network. *J. Am. Chem. Soc.* **2008**, *130*, 10996–11004.
- (53) Wu, Z.-P.; Miao, B.; Hopkins, E.; Park, K.; Chen, Y.; Jiang, H.; Zhang, M.; Zhong, C.-J.; Wang, L. Poisonous Species in Complete Ethanol Oxidation Reaction on Palladium Catalysts. *J. Phys. Chem. C* **2019**, *123*, 20853–20868.
- (54) Mostafa, S.; Behafarid, F.; Croy, J. R.; Ono, L. K.; Li, L.; Yang, J. C.; Frenkel, A. I.; Cuenya, B. R. Shape-Dependent Catalytic Properties of Pt Nanoparticles. *J. Am. Chem. Soc.* **2010**, *132*, 15714–15719
- (55) Ma, X.-Y.; Chen, Y.; Wang, H.; Li, Q.-X.; Lin, W.-F.; Cai, W.-B. Electrocatalytic Oxidation of Ethanol and Ethylene Glycol on Cubic, Octahedral and Rhombic Dodecahedral Palladium Nanocrystals. *Chem. Commun.* **2018**, *54*, 2562–2565.

☐ Recommended by ACS

Three-Dimensional Plasmonic Photocatalyst Consisting of Faceted Gold Nanoparticles and Radial Titanium(IV) Oxide Heteromesocrystals

Ryota Kojima, Hiroaki Tada, et al.

FEBRUARY 02, 2023

THE JOURNAL OF PHYSICAL CHEMISTRY C

RFAD 🗹

NiAl-LDH-Modified Core-Shell Rod-like ZnO@ZnS Heterostructures for Enhanced Photocatalytic Hydrogen Precipitation

Bochao Ma, Peipei Yang, et al.

FEBRUARY 06, 2023

THE JOURNAL OF PHYSICAL CHEMISTRY C

READ 🗹

Regulation of the B Site at $La(Ni_{0,1})MnO_3$ Perovskite Decorated with N-Doped Carbon for a Bifunctional Electrocatalyst in Zn-Air Batteries

Weiyi Shi, Jie Zhang, et al.

JANUARY 31, 2023

INDUSTRIAL & ENGINEERING CHEMISTRY RESEARCH

READ 🗹

Achieving Record-High Photoelectrochemical Photoresponse Characteristics by Employing Co₃O₄ Nanoclusters as Hole Charging Layer for Underwater Optical Communication

Yang Kang, Haiding Sun, et al.

FEBRUARY 08, 2023

ACS NANO

READ 🗹

Get More Suggestions >